PROPAGATION OF LIGHT IN STRONGLY DISORDERED PHOTONIC MATERIALS AND RANDOM LASERS

P. LODAHL#, G. VAN SOEST*, J. GÓMEZ RIVAS*, R. SPRIK* AND A. LAGENDIJK#

Department of Applied Physics and MESA+ Research Institute, University of Twente, P.O. Box 217, 7500 AE, Enschede, The Netherlands.

AND

* *Van der Waals-Zeeman Institute, University of Amsterdam, Valckenierstraat 65, 1018 XE Amsterdam, The Netherlands.*

1. Introduction

The quest for developing ever stronger interacting photonic materials has caused the birth of a widely expanding research field. Successful achievement of very strong elastic interaction between light and matter would allow demonstration of fundamental new physical phenomena, among which Anderson localization [1] and a full photonic bandgap [2, 3] are prime examples. Experimental realization of these phenomena would open new avenues in control and manipulation of light and matter [4], and could lead to fascinating new developments in quantum optics.

Several parameters determine the quality of a photonic material depending on the application. The interaction of light and the photonic material is mediated by scattering, and strong scattering is ensured by having a high refractive index contrast of the scattering particle with respect to the background material. Furthermore, the particle size of the scatterer relative to the wavelength of light is critical. Most efficient interaction is found in the Mie scattering regime where the size of the scatterer is comparable to the wavelength. Finally, the amount of optical absorption present in the photonic material often turns out to be a sensitive parameter that may hamper the observation of the delicate interference phenomena.

An alternative way of tuning the optical properties of a multiple scattering media is to add optical gain. This can be done for instance by doping the material with active molecules. The inclusion of gain induces a variety of new phenomena [5, 6]. In the case of a random multiple scattering media a threshold for lasing action and frequency narrowing can be observed. For that reason the systems have been called random lasers. This point of view is further supported by recent measurement proving that the photon statistics of a random laser is poissonian above threshold [7].

In the current contribution we will present recent experimental work on multiple light scattering in strongly photonic materials. The first part concerns porous gallium phosphide which is the strongest scattering medium for visible light reported to date. It is demonstrated how the photonic strength can be tuned sensitively during sample preparation by controlling the etching potential and the density of impurities in the sample. In the second part of the paper light propagation in random lasers is discussed. Experimental investigations of speckle statistics and enhanced backscattering in random lasers are supplemented by a new rate-equation model that explains the observations convincingly.

2. Fabrication and tuning of strongly scattering porous gallium phosphide

Recently a new strongly interacting photonic material was developed: porous gallium phosphide (GaP) [8]. It was realized that electrochemical etching of bulk GaP could provide a highly isotropic random network of holes making this porous structure an excellent candidate for experiments on light localization [9]. The high refractive index of GaP ($n = 3.3$) and the remarkable observation that optical absorption is undetectable in the samples give great promises. Furthermore, the physical size of the scatterers can be varied in the fabrication process which allows sensitive tuning of the photonic strength of GaP. In the current paper a detailed description of the electrochemical etching process of GaP is given, and measurements of the photonic strength are presented. A recent publication concerned the dependance of the photonic strength on the dopant density of the n-type GaP crystals [10]; here it is demonstrated that the etching potential V provides another important handle for tuning.

2.1. ELECTROCHEMICAL ETCHING OF GALLIUM PHOSPHIDE

Bulk n-type GaP can be etched electrochemically generating random porous structures. This etching occurs through the following chemical reaction of

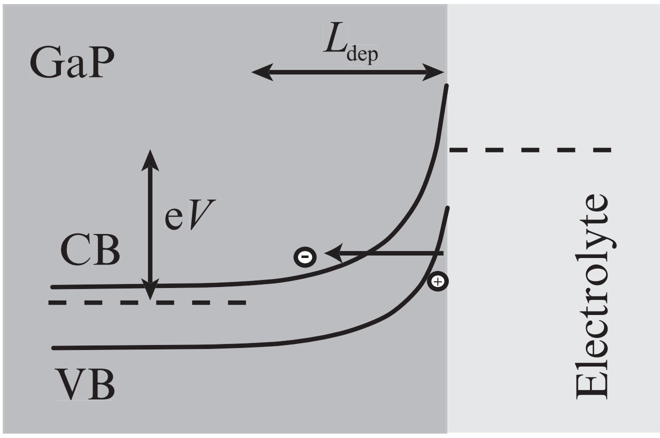

Figure 1. Interface between GaP and the electrolyte at a potential V. Electrons in the depletion layer L_{dep} may tunnel from the valence band (VB) to the conduction band (CB). The generated holes are used for the dissolution of the semiconductor at the interface.

GaP in an acid electrolyte

$$(\mathrm{GaP})_{\mathrm{n}} + 6\mathrm{h}^{+} \rightarrow (\mathrm{GaP})_{\mathrm{n}-1} + \mathrm{Ga}^{3+} + \mathrm{P}^{3+} \ . \tag{1}$$

This process requires the presence of valence-band holes that can be generated by applying a strong positive electric potential V on the semiconductor. This induces bending of the valence and conduction bands close to the semiconductor-electrolyte interface, c.f. Fig. 1. Hence electrons can tunnel from the valence to the conduction band generating valence band holes to drive the etching reaction (1). The region of bending of the valence and conduction bands is referred to as the depletion layer and has a spatial extent given by [11]

$$L_{\mathrm{dep}} = \left(\frac{2\epsilon\epsilon_0}{\mathrm{e}N}(V - V_{\mathrm{fb}}) \right)^{1/2} \ , \tag{2}$$

where $\epsilon = 11$ is the dielectric constant of GaP, ϵ_0 is the vacuum permittivity, e is the electron charge, N is the donor concentration, and V_{fb} is the flat-band potential. For a given semiconductor electrode, the flat-band potential depends mainly on the nature of the electrolyte. In our experiments (aqueous 0.5M H_2SO_4 solution) we have $V_{\mathrm{fb}} \simeq -1.2$ V [12].

It is important to investigate in detail how the porous structure is formed during the etching since this provides valuable knowledge about how to control the process. We used 300 μm thick commercially available GaP wafers doped with different concentrations of sulfur impurities. The etched

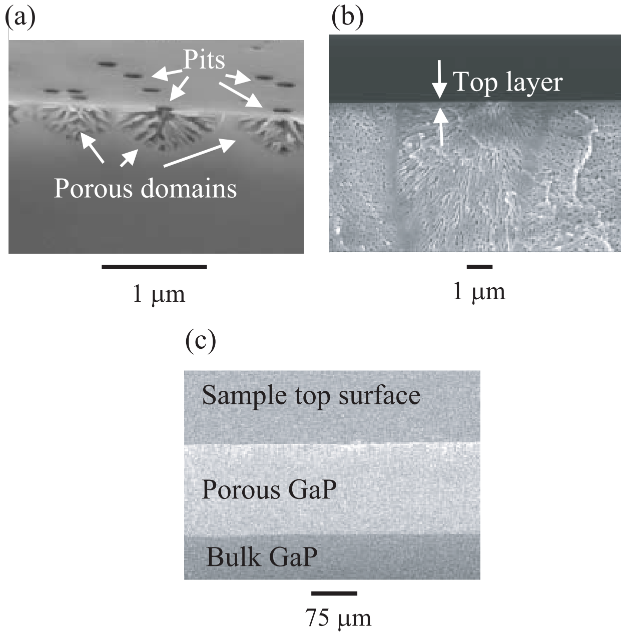

Figure 2. Electron-microscope (SEM) photographs of porous GaP. (a) cleaved cross section of a sample in which etching was stopped at its initial stage. (b) side view of a porous structure. (c) cleaved cross section of a layer of porous GaP with a thickness of 203 μm.

porous structure was studied with high resolution SEM images, where typical examples are displayed in Fig. 2. The etching is seen to start at specific pits on the surface where defects are present. These surface defects may lead to a local enhancement of the electric field helping the hole generation [12]. The pits can be clearly seen in the SEM photograph (a) of Fig. 2. This image shows a cleaved cross section of a porous GaP sample in which etching was stopped at the initial stage. From an initial pit a pore is formed. This pore branches leading to a porous domain that expands hemispherically. The porous domains, originating from different surface defects, can be seen in Fig. 2 (a). Once the adjacent porous domains meet, a porous layer grows at a constant rate. The SEM photograph of Fig. 2 (b) corresponds to a side view of a fully etched porous structure, while Fig. 2 (c) is a cleaved cross section, on a larger spatial scale, of a porous GaP layer. We observe that there is a thin layer of bulk GaP on top of the porous structure, with only a few pits remaining where the pore formation was initiated (see Figs. 2 (a) and (b)). The presence of this top layer complicates the analysis of optical experiments on porous GaP substantially and can advantageously be removed by photochemical etching [13].

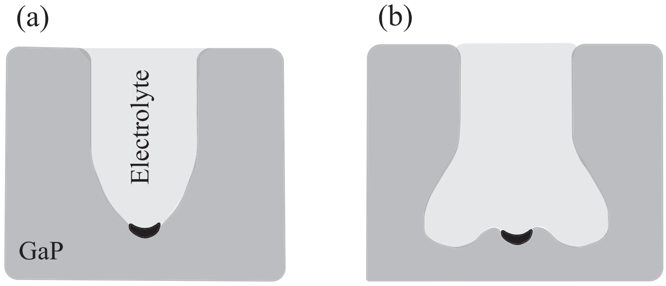

Figure 3. Schematic representation of the pore branching. Figure (a) represents a pore. The strongest electric field is at the pore tip due to the large curvature. The etching rate is higher in this region and it can be passivated, as represented by the black area. (b) shows how the etching can proceed in the non-passive region leading to the branching of the pore.

2.2. PHOTONIC STRENGTH

The strength of the photonic coupling between light and material is quantified by the scattering mean free path ℓ_s, which is the average distance between two consecutive scattering events. To the lowest order approximation, i.e. in the independent scattering approximation, the scattering mean free path is given by

$$\ell_s = \frac{1}{\rho \sigma_s}, \tag{3}$$

where ρ is the density of scatterers and σ_s is the scattering cross section. Strong scattering is achieved by optimizing both ρ and σ_s. In our samples the density of scatterers is determined by the inter-pore distance d_p and the radius of the pores r, while the scattering cross section depends solely on the pore radius. These parameters can be tuned by controlling the etching potential and the doping concentration. The latter dependence was investigated in depth in [10], while we in this section present measurements on the photonic strength versus etching potential.

The inter-pore distance d_p in electrochemically etched n-type semiconductors is determined by the extent of the depletion layer L_{dep} [12, 14, 15]; and this distance is always smaller than $2L_{\text{dep}}$. If the depletion layers of adjacent pores overlap, the electric field is reduced and the etching stops. The dissolution process only occur in regions where the field is enhanced. These regions are the pore tips where the enhancement of the field is highest due to the radius of curvature. Above a critical etching rate, the reaction (1) may be locally passivated, as limited by oxidation. However, the etching can proceed close to the pore tip causing a branching of the pore and eventually the formation of the random network structure. This branching

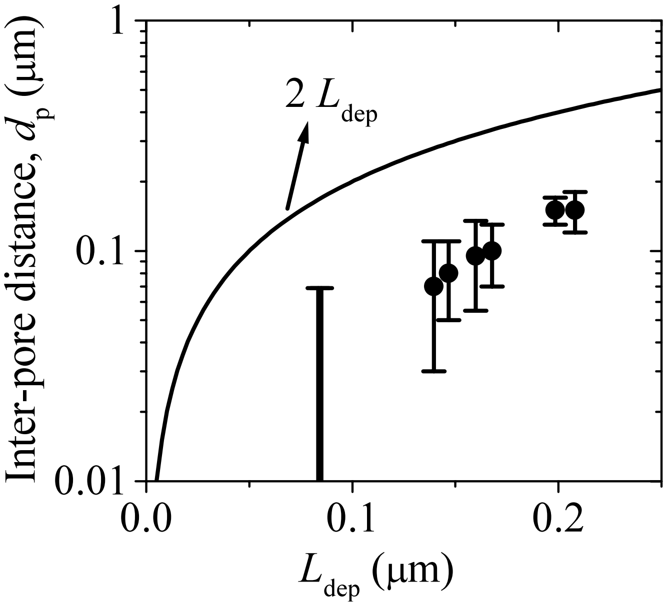

Figure 4. Inter-pore distance in porous GaP versus the extent of the depletion layer $L_{\rm dep}$. The solid line represents $2L_{\rm dep}$.

process is summarized in Fig. 3. Figure 4 shows the inter-pore distance of porous GaP plotted as a function of $L_{\rm dep}$. The inter-pore distance is defined as the average distance between adjacent pore walls, as was estimated with a marked gauge from high magnification SEM images. As expected we observe that the pore distance increases with the extent of the depletion layer and that $2L_{\rm dep} \geq d_p$, where $2L_{\rm dep}$ is marked with a solid curve in Fig. 4.

As discussed in Ref. [15], the extent of the depletion layer also determines the average pore radius in n-type semiconductors. Larger pores are formed when $L_{\rm dep}$ is increased. Note that $L_{\rm dep}$ depends on the applied potential during etching (see Eq.(2)). Therefore both the inter-pore distance and the pore radius will be changed when varying V, i.e., both the density of scatterers and the scattering cross section are changed. It will be shown below that increasing the potential V will lead to stronger scattering. This implies that the dominating contribution is the increased scattering cross section that overwhelms the reduction from the decrease in scatterer density.

A direct measurement of ℓ_s in strongly scattering samples is very intriguing due to the exponential decay of coherent transmission with the sample thickness [16]. Therefore, we extract the scattering strength from enhanced backscattering (EBS) measurements [17]. The width of the EBS cone is inversely proportional to the transport mean free path ℓ, defined as the average distance the light travels in the medium before the propagation direction is completely randomized [18]. In general the transport mean free path ℓ is larger than ℓ_s, and the two quantities only coincide in a medium formed by isotropic scatterers.

Figure 5 shows results of EBS measurements on two porous GaP samples with $N = 5 \times 10^{17}\text{cm}^{-3}$, etched at 15 V (squares) and at 16.6 V (circles). The latter is the highest potential at which etching is possible. Above this potential the GaP electrode is passivated and etching stops. The EBS cone of the sample etched at the high potential is significantly wider, indicating stronger scattering. The extracted transport mean free paths are $\ell = 0.22 \pm 0.02\mu$m (for the sample etched at 16.6 V) and $\ell = 0.43 \pm 0.03\mu$m (for the sample etched at 15 V), as obtained from the fits of the EBS cones using diffusion theory [19] (the solid lines in Fig. 5). Internal reflection at the surface of the material was included in the fits with values of the effective refractive index obtained by measuring the angular-resolved transmission [20]. These measurements promotes porous GaP to the strongest scattering elastic media for visible light found to date.

We note that the measurements of the transport mean free path are consistent with the average pore radius of the samples extracted from SEM images. The sample etched at 15 V has an average pore radius $r = 0.05 \pm 0.02\mu$m while the sample etched at 16.6 V has $r = 0.095 \pm 0.02\mu$m. Thus, increasing the etching potential implies a structure with larger pores that scatters light more effectively since the pore radius approaches the wavelength of light. The inter-pore distance is found to be the same for the two different etching potentials within the error bars of our measurements ($0.15 \pm 0.03\mu$m).

2.3. CONCLUSIONS

Electrochemically etched porous GaP is the strongest scattering medium reported for visible light. Understanding the etching process allows tailoring the scattering strength of the materials. Important tuning parameters are the etching potential and the doping concentration in the GaP wafer. In this section a detailed account for the etching process was given and the tuning characteristics were investigated. Based on enhanced backscattering measurements the transport mean free path was extracted. The detailed control of the etching process should allow future preparation of even stronger scattering samples potentially reaching the boundary for Anderson localization. The lack of detectable optical absorption in GaP would hopefully allow clear studies of the onset of localization.

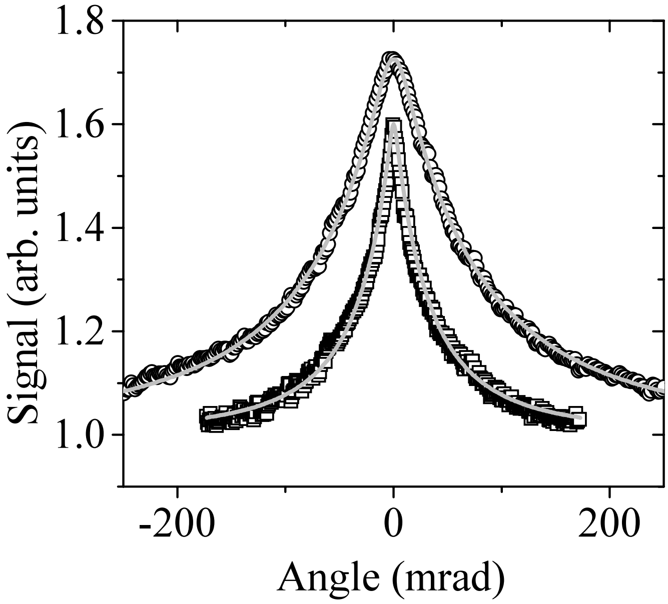

Figure 5. EBS measurements of porous GaP ($N = 5 \times 10^{17}$ cm^{-3}) anodically etched at 15 V (squares) and at 16.6 V (circles). The solid lines through the symbols are fits using diffusion theory.

3. Propagation of Light in Random Lasers

Random lasers are strongly scattering media with optical gain. These systems have many features in common with more conventional lasers based on an optical gain medium enclosed in a cavity to enhance stimulated emission. For example, a threshold for lasing action and associated frequency narrow emission have been observed in random lasers based on multiply scattering colloidal dispersions in dyes [6, 21]. Evidently the optical properties of random lasers are quite different from conventional lasers: the propagation of pump and fluorescence light is diffusive, and there is no "preferred direction" in feedback and loss processes. The ambiguities as to what exactly constitutes the loss in a random laser, how optical feedback works if it is non-directional, and the theoretical prediction of an intensity divergence will be discussed in the following. Experimental clarification is obtained by measuring speckle statistics and enhanced backscattering from a random medium with gain.

3.1. TRANSPORT EQUATIONS FOR LIGHT IN A RANDOM LASER

Gain in a multiple scattering medium can be included directly in the diffusion equation

$$\frac{\partial W}{\partial t} = D\nabla^2 W + \kappa_{\rm g} W + S\,, \tag{4}$$

where W is the energy density of the light, D the diffusion constant for light in the medium, $\kappa_{\rm g}$ is the gain coefficient, and S the source term. Solutions of Eq. (4) exist only for a finite sized system [5]. The maximum volume for which a solution can be found is called the critical volume $V_{\rm cr}$. The physical origin of this behavior is the existence of infinitely long diffusive paths which will be amplified to infinite intensities in a gain medium. This results in a diverging intensity whenever the probability for a path to be scattered out of the system is compensated by the gain. Chances of leaving the medium are smaller for larger systems, so the smaller the gain the larger $V_{\rm cr}$. The critical thickness is $L_{\rm cr} = \pi\sqrt{\ell\ell_{\rm g}/3}$, where ℓ the mean free path for scattering and $\ell_{\rm g}$ the gain length.

Eq. (4) is not sufficient to describe the lasing and threshold behavior of a random laser in general, hence the temporal and spatial dependence of the light fields must also be considered. A simple set of equations including these effects is given by [22, 23]

$$\begin{aligned}
\frac{\partial W_\ell}{\partial t} &= D\nabla_z^2 W_\ell + \left(\sigma_{\rm e} c n_1 - \sigma_{\rm r} c n_0\right) W_\ell + \frac{\beta}{\tau} n_1, \\
\frac{\partial W_{\rm p}}{\partial t} &= D\nabla_z^2 W_{\rm p} - \sigma_{\rm a} c n_0 W_{\rm p} + \frac{1}{\ell} I_{\rm in}, \\
\frac{\partial n_1}{\partial t} &= \sigma_{\rm a} c n_0 W_{\rm p} - \left(\sigma_{\rm e} c n_1 - \sigma_{\rm r} c n_0\right) W_\ell - \frac{1}{\tau} n_1.
\end{aligned} \tag{5}$$

Here W_ℓ and $W_{\rm p}$ are the space and time dependent “laser” and pump light densities where the spatial dependence has been restricted to 1D as expressed by the z-coordinate. Intensity W_ℓ represents only the light taking part in the amplification process; not all the emitted luminescence. The parameter β in Eqs. (5) is the fraction of spontaneous emitted light contributing to the laser light [24]. The ground state and excited state populations are n_0 and n_1, satisfying $n_0 + n_1 = n$, the total dye concentration. The cross-sections $\sigma_{\rm e}, \sigma_{\rm a}$, and $\sigma_{\rm r}$ describe emission, absorption, and reabsorption of the laser and pump light. Finally, τ is the relaxation time for spontaneous emission, and c is the speed of light in vacuum.

Eqs. (5) can be solved numerically (see [22, 25] for details) to obtain insight in the coupling between the diffusive part and the level dynamics. A characteristic example is given in Fig. 6. The dependence of the dynamic quantities on the position in the medium shows that only a relatively thin

($< 10\ell$) layer develops with significant population inversion at the arrival of a pump pulse. This layer provides the net gain and also serves as a source for spontaneous emission. The z-dependence of the inversion: n_1 is exponential and non vanishing only where the pump light can reach it through the absorbing and scattering medium.

The spatial and temporal dependence of the population inversion has an immediate influence on the gain that probe light will experience when diffusing through the medium. We will show in section 3.3 how this influences enhanced backscattering in a medium with gain. A close investigation of the temporal behavior reveals [22] that the dynamics of a random laser is very similar to those of a conventional laser system. For instance the relaxation oscillations [26] observed after arrival of a pump pulse (see Fig. 7) are well known in conventional lasers. The relaxation oscillation dynamics is found to force the system towards a well defined equilibrium, thus resolving the divergence problem found in the diffusion equation Eq. (4). The random laser threshold we find is obtained from a transport formalism taking into account the local gain in a population rate equation. This shows that the "laser view" [27, 28, 29, 30] and the "multiple scattering view" [31, 32, 33, 34] on random lasers can be united into one. We note that the conclusions presented here are in agreement with other theoretical work (see, e.g., [5, 27, 29, 35, 36, 37]) based on diffusive transport and gain dynamics obtained by, e.g., Monte Carlo calculations including spectral dependence. Recent observations of sharp spikes in the emission spectrum of random lasers [38] could be due due to interference effects in the scattering medium [39]. Interference effects are not included in Eqs. (5), but are discussed in e.g. the contributions of Soukoulis and Sabbah in this school [40].

3.2. SPECKLE IN RANDOM LASERS

Speckle is the strongly fluctuating, grainy intensity pattern resulting from the interference of a randomly scattered coherent wave. It can be observed in space, time, and frequency. Some statistical characteristics of the speckle pattern contain information about the transport process [41]. We discuss here only spatial speckles, recorded as the fluctuating intensity versus emission angle.

If a coherent plane wave falls on a rough surface, a speckle pattern can be seen on a screen positioned at some distance from the scattering object. The observed intensity $I = |E|^2$ follows a Rayleigh distribution

$$P(I) = \frac{1}{\langle I \rangle} e^{-\frac{I}{\langle I \rangle}} \,. \tag{6}$$

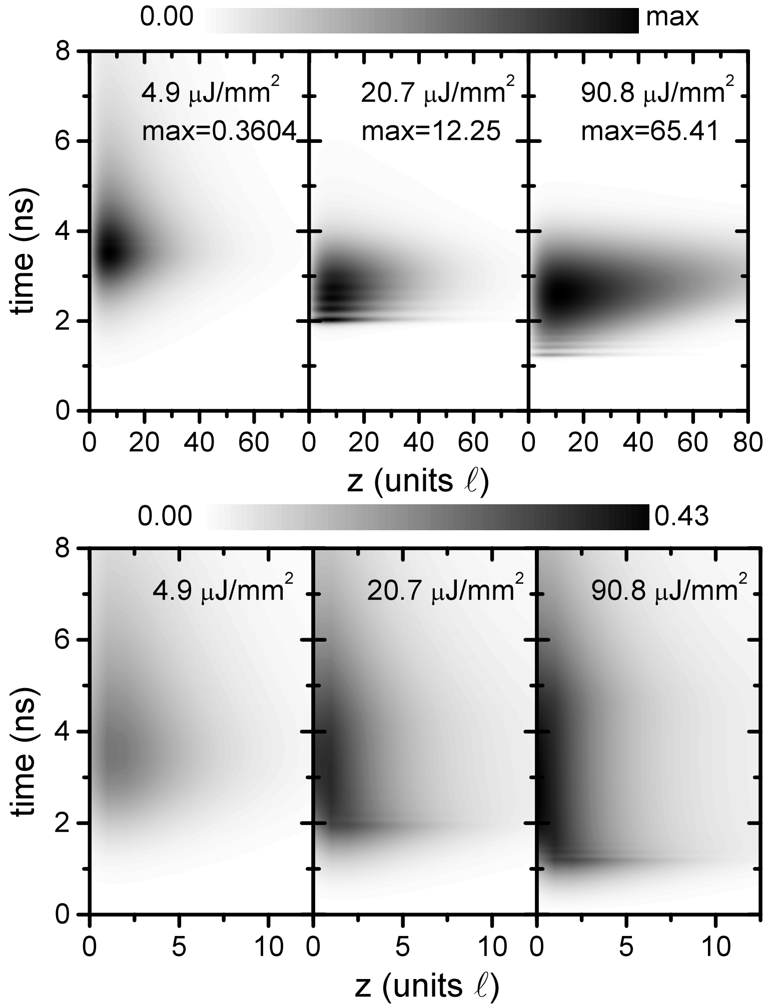

Figure 6. Simulation results of Eqs.5 for a parameter choice characteristic for Sulforhodamine B in titania dispersions [25]. Top: Density of laser light $\tilde{w}_\ell = W_\ell/(\sigma_e c\tau)$ in a random laser as a function of time t (vertical axis) and position z (horizontal axis) for the three different pump fluences indicated in the figures. The grayscale runs from zero to the maximum density (indicated in the plots). The threshold pump fluence is 10 μJ/mm^2. Bottom: Inversion n_1/n in a random laser as a function of time t (vertical axis) and position z (horizontal axis) for the three different pump fluences indicated in the figures. The maximum inversion obtained for above threshold pump fluences (> 10 μJ/mm^2) is about 0.43.

The typical speckle spot size depends on the characteristic distance along the screen on which the fields that contribute to the speckle dephase. The largest path length difference at a spot on the screen is caused by the partial waves arriving from opposite ends of the illuminated region of the

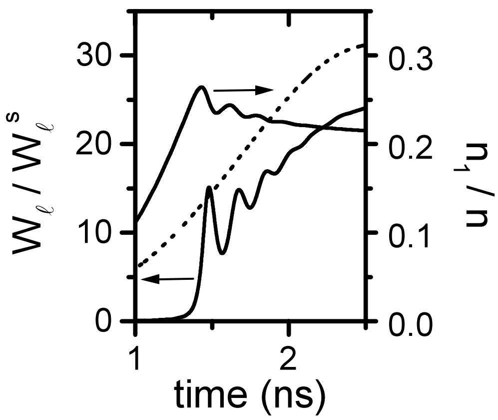

Figure 7. Close-up of the relaxation oscillation for a pump fluence of 53.6 μJ/mm^2.

scattering surface. Consequently, the typical angular size of a speckle spot is λ/d [42], if d is the diameter of the illuminated region.

The field of speckle experiments in random lasers is largely uncharted territory. The only data available of the effect of gain on a speckle pattern produced by a probe beam are those of ref. [43]. Refs. [44] and [45] study the related subject of coherence properties of the generated light. Recent measurements by Cao et al. [7] used speckle characteristics to determine the coherence of light from a random laser. In this section we present our experimental results concerning the intensity statistics and speckle spot size. In contrast with passive systems, these measurements do depend on the parameters of light transport.

3.2.1. *Sample and setup*

We work with a setup in which the pump and probe pulses are incident simultaneously on the sample (see Fig. 8). The light in the medium then consists of amplified probe light, in which we are interested, and fluorescence. Since it is favorable to do the experiments at large amplification, and the maxima of the gain curve $\sigma_e(\lambda)$ and the fluorescence spectrum $L(\lambda)$ of dye are usually close in wavelength, the probe and fluorescence can not be separated spectrally or temporally. However, the coherence and the associated speckle pattern are different and will be used to discriminate between fluorescence and amplified light.

The pump and probe pulses are produced by one laser system consisting of an optical parametric oscillator (OPO) pumped by a Q-switched Nd:YAG laser (see section 3.3.1). For the speckle experiment we probe with the output of the OPO at 480 nm, and the residual doubled Nd:YAG light at 532 nm is used as pump. The samples consist of titania suspensions

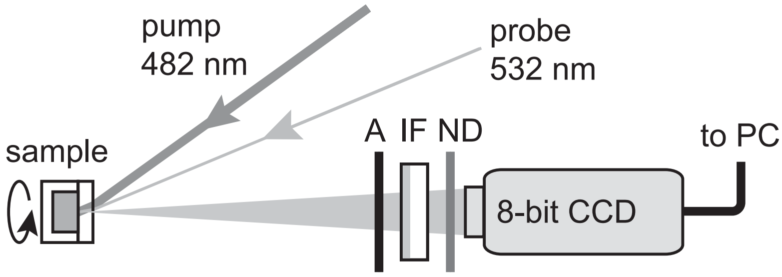

Figure 8. Schematic of the setup for speckle experiments. The pump (diameter 2 mm) and probe (diameter 0.8 mm) reach the sample simultaneously. The sample is mounted on a motor, spinning it slowly to prevent sedimentation. The scattered and amplified probe light is collected on an 8-bit 752×582 pixel CCD camera (Kappa CF 8/1 FMC), through an aperture (A), a 532 nm interference filter (IF), and one or more neutral density filters. The distance between sample and camera is 10 cm.

doped with 2 mM Coumarin 6 dye. The suspension is contained in a round plastic container with dimensions 6 mm depth $\times$ 10 mm diameter, covered with a 4 mm thick glass window. The sample is rotating slowly to prevent sedimentation and dye degradation. The transport mean free path of the sample is found be 10 μm from enhanced backscattering measurements. The threshold pump intensity is $I_{\mathrm{p}} = 0.22$ mJ/mm^2.

The speckle is recorded on a Kappa CF 8/1 FMC 8-bit CCD camera. The light from the sample passes through an aperture, blocking stray light, a 532 nm interference filter with a transmission FWHM of 1.0 nm to remove most of the fluorescence, and a neutral density filter. The image is a single shot exposure, because the liquid suspension leads to continuous speckle changes. The probe beam diameter is 0.8 mm. This produces a speckle that can be resolved well on the camera, with a large number of speckle spots. The pump spot is chosen to be larger, 2 mm, to provide a large amplifying region for the probe light to propagate in. Figure 8 is a schematic of the experimental arrangement of sample and detection.

3.2.2. *Intensity statistics*

The Rayleigh distribution of speckles is a very robust phenomenon. As such, measurements of the speckle intensity statistics is not an effective method to obtain new information about random lasers. It However, it does provide a measurement of the degree of amplification of the incident probe, a property that is otherwise difficult to quantify.

We make use of the coherence of the Nd:YAG frequency doubled output as a probe pulse, producing a speckle with good visibility. Figure 9(a) shows an image of the speckle pattern in scattered and amplified probe light from a Coumarin6/TiO_2 random laser. The drawback of the large pump spot is

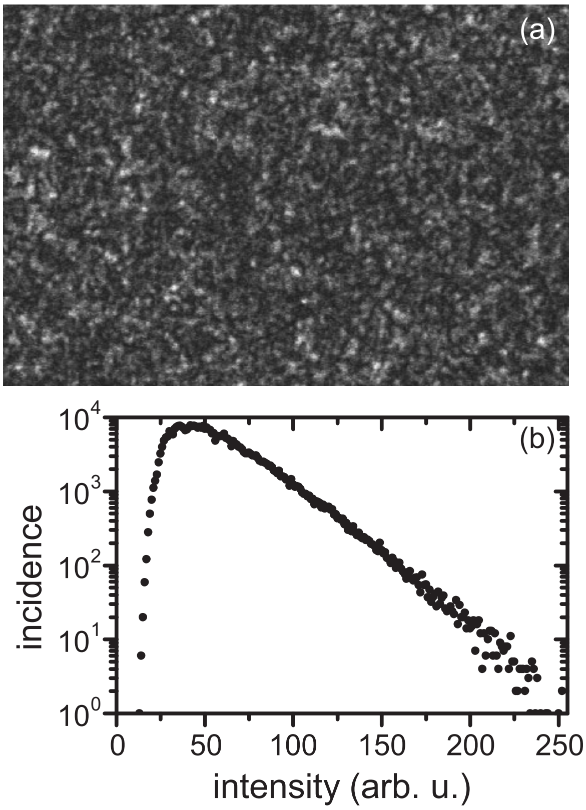

Figure 9. *(a)* Speckle pattern on an 8-bit CCD camera of frequency-doubled Nd:YAG scattered and amplified by a 2 mM Coumarin 6 solution in hexylene glycol with TiO_2 scatterers, $\ell = 10\ \mu$m. The pump pulse from the OPO of wavelength 482 nm has an energy of 0.32 mJ/mm^2. *(b)* Intensity histogram of the image in *(a)*. The Rayleigh distribution is offset by a background of incoherent fluorescence. The slope of the linear decrease is $1/\langle I \rangle$.

a larger fluorescence component in the image.

The intensity histogram of the speckle in Fig. 9(a) is shown in Fig. 9(b). The histogram has an unusual feature: it only starts to show Rayleigh statistics above intensity 50. The lower intensities are incoherent fluorescence, giving each pixel an offset. The average intensity can be determined from the slope of the exponential decrease for higher intensities.

We extract the average intensity of the amplified probe from the slope of the intensity statistics plotted in the manner of Fig. 9. The dependence of the average intensity of the speckle, or the intensity of the amplified probe, on pump fluence is plotted in Fig. 10.

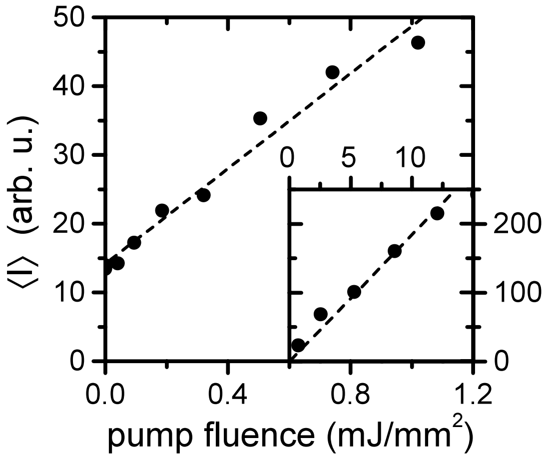

Figure 10. Average intensity derived from Rayleigh statistics as a function of pump fluence for a fixed probe intensity of 59 μJ/mm^2. The amplified intensity grows linearly with pump fluence. For comparison, we plot the mean intensity as a function of the *probe* fluence (in units of 0.01 mJ/mm^2) in the inset. The pump intensity is high: 2.9 mJ/mm^2. The lines are linear fits to the data.

3.2.3. *Speckle spot size*

A measurement of the speckle spot size yields the transverse dimension of the coherent source on the scattering surface. In a random laser this may very well depend on the pump energy, since a larger gain allows the light to spread further, thus enhancing long paths.

The spot size is measured by calculating the two-dimensional intensity autocorrelate $G_{\mathrm{I}}(\Delta\theta) = \langle I(\theta)I(\theta+\Delta\theta)\rangle$ of a speckle pattern as in Fig. 9(a). The contrast between the maximum at zero and the value at large $\Delta\theta$ is a factor 2: $G_{\mathrm{I}}(\Delta\theta \gg \lambda/d) = \langle I\rangle^2$, and $G_{\mathrm{I}}(0) = 2\langle I\rangle^2$.

The diffuse light source is partly incoherent due to the contribution of fluorescence. The consequences for the intensity autocorrelate are shown in Fig. 11, showing a cross section through the autocorrelate of the data in Fig. 9(a). The speckle contrast is reduced [46] to $1 + (\langle I\rangle/\langle I_{\mathrm{T}}\rangle)^2$, where $\langle I\rangle$ is the average intensity of the amplified probe and $\langle I_{\mathrm{T}}\rangle = \langle I\rangle + I_{\mathrm{F}}$ is the average total intensity, including the fluorescence intensity I_{F}. For the data in Fig. 9 $\langle I\rangle \approx I_{\mathrm{F}}$ and so the contrast in the autocorrelate is reduced to a factor 1.25.

The resulting $G_{\mathrm{T}}(\Delta\theta)$ $(= G_{\mathrm{I_T}}(\Delta\theta))$ is normalized to $\langle I_{\mathrm{T}}\rangle$ and analyzed quantitatively by modelling it with a function

$$G_{\mathrm{m}}(\Delta\theta) = 1 + \left[\frac{\langle I\rangle}{\langle I_{\mathrm{T}}\rangle}\right]^2 e^{-\Delta\theta/\theta_{\mathrm{c}}} \,. \tag{7}$$

$\langle I\rangle$ and $\langle I_{\mathrm{T}}\rangle$ are determined directly from the data, so θ_{c} is the only free

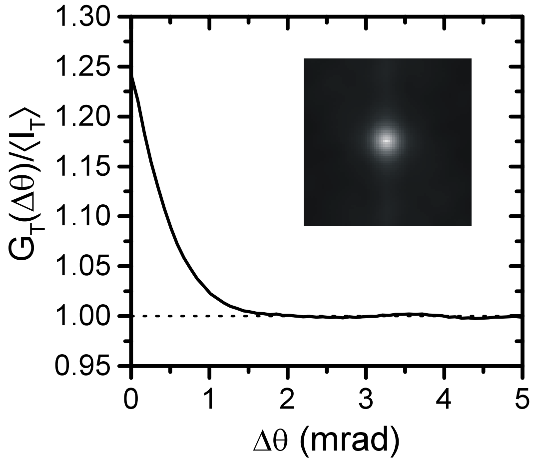

Figure 11. A cross section through the autocorrelate $G_{\mathrm{T}}(\Delta\theta)$ of the data in Fig. 9, normalized to the average total intensity $\langle I_{\mathrm{T}}\rangle$. The contrast is reduced from 2 to 1.25 due to the incoherent background. The two dimensional autocorrelate itself is shown as the inset.

parameter in a fit to G_{m}, providing a way to determine the speckle spot size.

In Fig. 12(a) θ_{c} is plotted as a function of pump fluence. The speckle spots are found to shrink as the pump fluence is increased from 0 to 1 mJ/mm^2, after which their size is approximately constant. The optical resolution of the imaging system is ≈ 0.1 mrad. Apparently the source of diffuse light producing the speckle becomes larger if the pump fluence is larger. This is consistent with the notion that mainly the long paths are amplified in a random laser. If only the intensity is increased, without actually changing the amount of amplification, the speckle size is constant, c.f. Fig. 12(b).

Without the pump, the speckle size is set by the probe beam diameter of 0.8 mm (80ℓ), and for the highest pump energies the equivalent source size increases to approximately 1.5 times this value. For high pump fluence the speckle does not get smaller. This is consistent with the result obtained in Section 3.1 with Eqs.(5).

3.3. ENHANCED BACKSCATTERING IN RANDOM LASERS

In this section we describe enhanced backscattering measurements that probe the gain dynamics in a random laser. We focus specifically on the laser threshold and experimentally investigating its role for the light propagation. Enhanced backscattering (EBS) has evolved from being a subject of study in itself [47] into a tool that can be utilized for studies of wave transport in

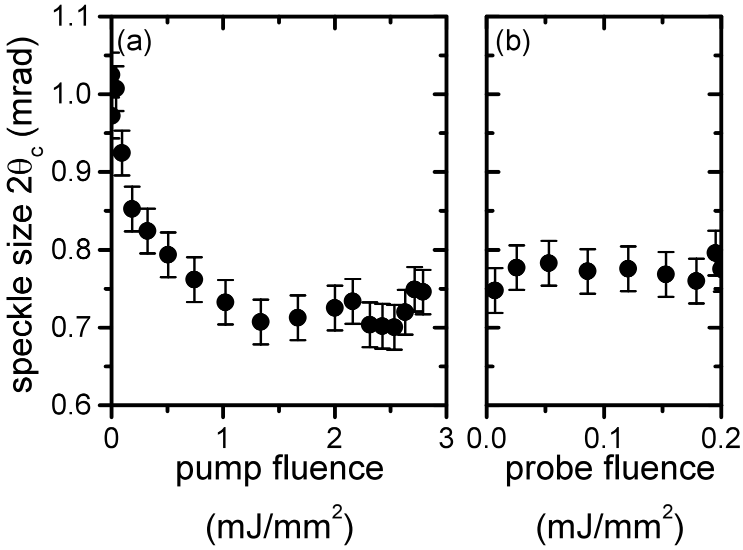

Figure 12. Characteristic decay angle of the autocorrelate. *(a)* For large pump fluence the speckle spots get significantly smaller compared to the case without gain, indicating that the amplification assists the spatial spreading of the probe light. The probe fluence is 59 μJ/mm^2. *(b)* The speckle size as a function of probe energy found to be constant for a fixed pump fluence of 2.9 mJ/mm^2, hence demonstrating the role of the amplification in *(a)*.

random media in a very precise and quantitative manner [9]. The shape of the backscatter cone is determined by the characteristic transport distance of the light in the medium. The exponential amplification of the intensity with path length in a gain medium results in a larger contribution of long light paths compared to light in passive material. The long light paths constitute the top of the EBS cone: a relatively larger contribution of long paths yields a sharper and narrower EBS line shape [32, 48]. This sensitivity to long paths makes EBS particularly well-suited for testing the alleged divergence behavior.

3.3.1. *Experimental details*

The setup is similar to the one used in the speckle experiment (see section 3.2). Our measurements of EBS in high gain amplifying random media are performed with samples consisting of 220 nm diameter TiO_2 colloidal particles suspended in 1.0 mM Sulforhodamine B laser dye in methanol. When measuring EBS it is important to average out the speckle, which has a much larger intensity variation than the cone, and so will obscure it. A source with short coherence length produces a speckle with less contrast, so it is easier to average. In this case the short coherence length of the OPO is

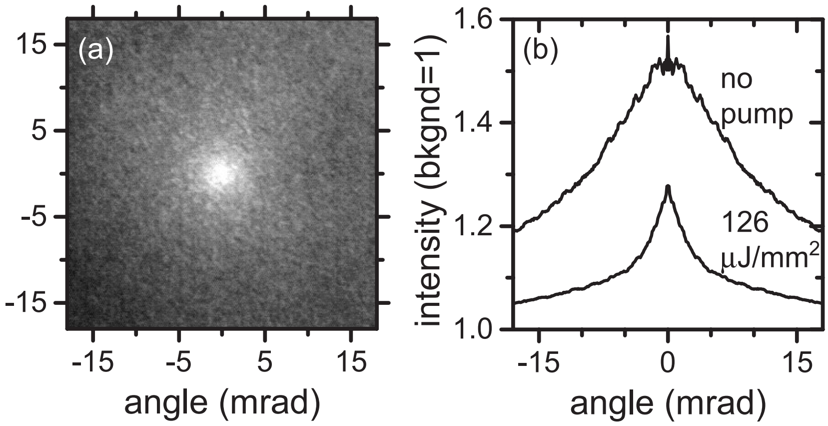

Figure 13. *(a)* CCD image of scattered probe light for a pump fluence of 126 μJ/mm^2. The exposure is the sum of 72 shots, averaging out most of the speckle. *(b)* The EBS cone derived from image (a) (bottom curve) by averaging over the azimuthal angle around the top. The resulting curve is mirrored around $\theta = 0$ and the background is normalized. For low intensities residual speckle may be a problem, especially around the top of the cone where the amount of pixels contributing to the average is small. As an example the cone without pump is shown (top curve). $E < 2$ due to single scattering, stray light, and fluorescence (c.f. Fig. 9(b)).

actually an advantage, and the use of the OPO allows us to take Sulforhodamine B as a gain medium, which is easier to work with than Coumarin 6. The scattered light is collected through an interference filter and a focusing lens on the CCD camera to record the EBS cone. We accumulate 51 to 204 different speckles (realizations) in each exposure, depending on the collected intensity. The angular resolution is 1 mrad, as limited by the probe beam divergence.

3.3.2. *Experimental results*

In Fig. 13 a typical example of a measurement is shown. The image clearly shows the larger intensity near the backscattering direction. For analysis we manually find the center of the peak and integrate on concentric circles around it. From the backscattering cone measured without pump, taking into account the reabsorption, we infer that the transport mean free path $\ell = 3$ μm. Earlier EBS experiments [32, 49] have been performed with materials in which the laser threshold could not be reached. In our sample the laser threshold is found to be at a pump fluence of 10 μJ/mm^2. The salient features of the influence of gain can be seen in Fig. 13. Both the width of the cone and the enhancement factor E become smaller with increasing pump energy. The enhancement factor has a (gain-independent) value of maximally 2 that is diminished by angle-independent contributions to the intensity. The cone width is related to the transport length: for a cone without gain it scales $\propto \ell^{-1}$, and this allows determination of the transport mean free path. The larger fraction of long light paths at high gain reduces the width of the EBS cone, but there appears to be no sign of a divergence or a sudden change in behavior at the threshold crossing. After the initial cone narrowing, the width saturates far above threshold at a value that is a third of the width of the cone without gain [25]. The decrease of E from 1.65 to 1.25 is due to the incoherent fluorescence component in the collected light, which becomes stronger for higher pump energies.

3.3.3. *Comparison with theory*

For a comparison with theory we need to extract EBS cones from the calculated time- and position-dependent gain profile data. The z-dependence of $\kappa_{\rm g}(z,t)$ in EBS can be treated with the method due to Deng *et al.* [50]. The basis is an expansion of a solution of the diffusion equation in eigenmodes leading to a static form factor of the EBS intensity $\gamma_E(\theta)$.

In the analysis of $\kappa_{\rm g}(z)$ the time variation is a subtle issue. The similarity of time scales of gain dynamics and light transport makes it very difficult to solve the time-dependent EBS cone in a varying gain-profile. Extending the method outlined above to $\kappa_{\rm g}(z,t)$ would mean that the ϕ_n and ε_n become time-dependent. We chose instead to use the averaging property by the time-integrated detection method in the experiment to simplify the analysis.

Since the EBS process itself samples the medium on the time scale needed to build up a cone, it only senses slow variations in $n_1(z)$. The longest paths that contribute in an experiment with an angular resolution of 1 mrad have a separation between entrance and exit points of $d = 10^3\lambda \approx 600$ μm. The diffusive transport time over this distance is $d^2/D \approx 1.7$ ns. We mimic this property by low-pass filtering the data, and subsequently averaging $n_1(z,t)$ in time windows of length d^2/D, and use this mean inversion profile to calculate a "partial" EBS cone. The partial cones are summed, each weighted with the mean probe intensity in its window. This procedure largely overcomes the dominance of the nearly critical $\kappa_{\rm g}(z)$ occurring in the relaxation oscillation: long paths, needed for the divergence to happen do not have the time to build up in the ≈ 50 ps that the "supercritical" inversion lasts. This demonstrates once again that the dynamic picture, although allowing for high inversion densities, prevents the explosion.

3.3.4. *Discussion*

The comparison between theory and experiment for EBS cones is displayed in Fig. 14. The agreement between experimental data and theoretical de-

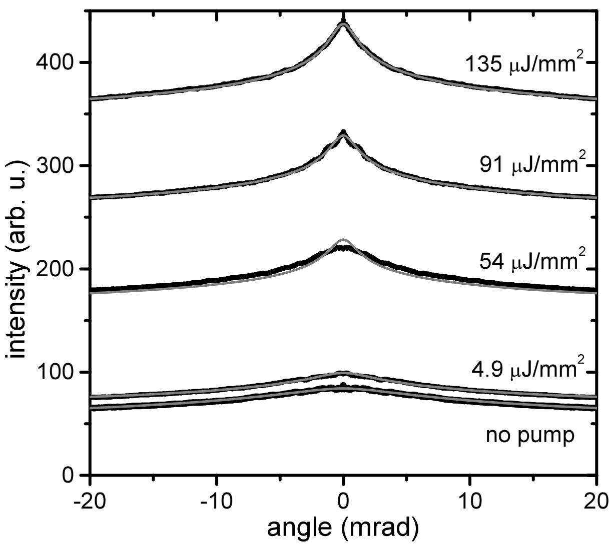

Figure 14. Black points: enhanced backscattering cones for pump fluences ranging from 0 to 135 μJ/mm^2. Gray lines: cones calculated from the dynamic theory. The experimental results are accurately reproduced by the theory, except for intermediate pump energies (approximately 20-70 μJ/mm^2; one example shown) where the relaxation oscillations dominate the temporal inversion profile.

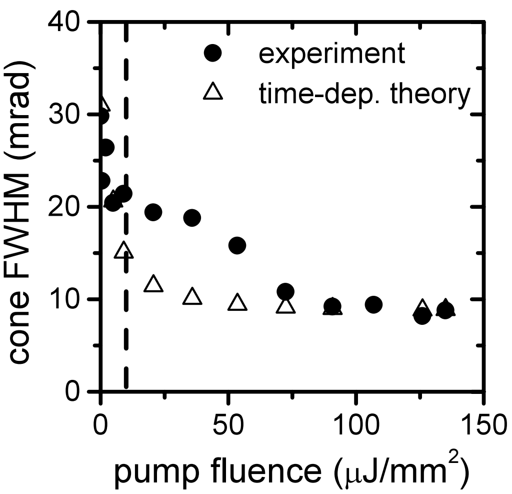

Figure 15. The full widths at half maximum of the backscatter cones as a function of pump fluence. The dashed line indicates the threshold obtained from an independent measurement. The circles are experimental data and the triangles are the corresponding results from simulations.

scription is excellent for low and high pump energies. Initially, the width of the EBS cone drops quickly with increasing pump pulse energy. Far above threshold, the FWHM saturates (at $\approx$ 10 mrad, depending on system parameters) due to the pump-independence of the above-threshold $n_1(z)$.

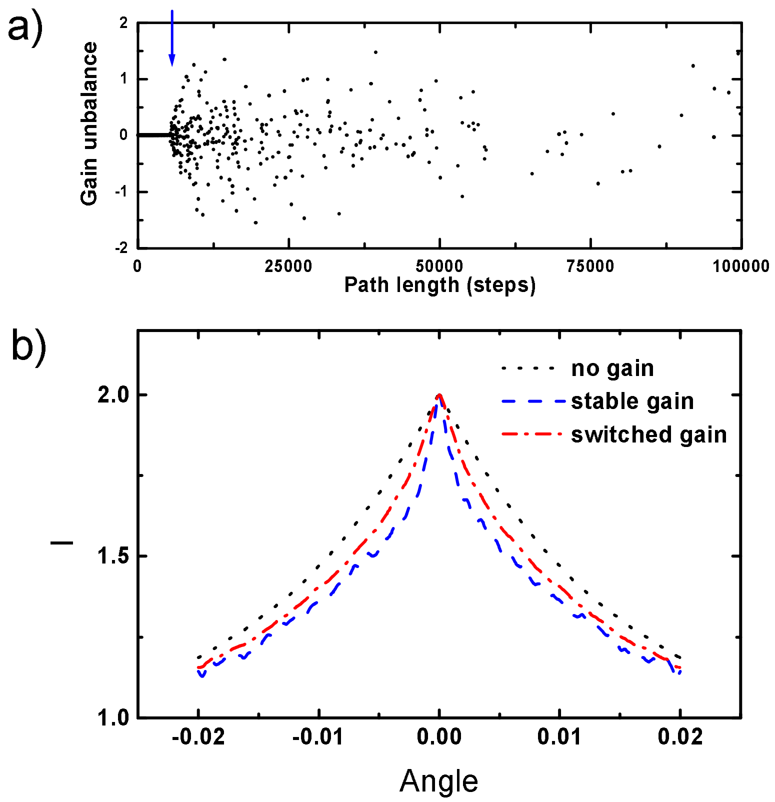

Figure 16. Simulation of the effect on EBS of a difference in gain profile for forward and reverse paths. a) Unbalance between the forward and backward gain for some paths generated by Monte Carlo. The gain was switched off after a time indicated by the arrow. b) The EBS for the medium without gain (dotted), a static gain (dash), and a switched gain (dash-dot).

For pump fluences between 20 and 70 μJ/mm^2 the theory deviates from the experimental results, see Fig. 15. This discrepancy is due to the entanglement of the time scales of transport and variation of $n_1(z)$. Since $n_1(z)$ changes faster than the time needed for the formation of a backscatter cone, the reversibility of transport in the medium is affected. A wave traversing the medium along a certain path experiences a spatiotemporal gain profile that is in principle different from the profile seen by the wave in the reversed path. This reduces the interference contrast in the scattered light, as the two waves no longer have equal amplitudes when exiting the medium. This unbalance is especially prominent just above threshold where the long-lived oscillations make up an important part of the temporal gain profile. Long light paths are most strongly influenced by changes in $n_1(z)$. Their interference contribution to the EBS is smaller than inferred from the averaged gain profile.

The effect can be seen qualitatively in the simulation presented in Fig. 16. In the simulation the dynamics of the gain medium is emulated by assuming a finite depth for the gain profile that switches off after a certain relaxation time. The path distribution is simulated by Monte Carlo generation and the overall difference in gain between forward and backward propagation along this path is evaluated. The gain difference is taken into account in accumulating the EBS shown in Fig. 16.b). The cone for the switched medium is wider than for the medium with a static gain profile, and still narrower than a medium without gain. A detailed comparison with the measurements requires a better description of the gain medium using the solutions of Eqs. (5).

Acknowledgements

We are grateful to F.J. Poelwijk for his help and discussions regarding our experiments on random lasers. Our work on porous GaP has profited considerably from the input of J. J. Kelly, R. W. Tjerkstra, and D. Vanmaekelbergh. This work is part of the research program of the Stichting voor Fundamenteel Onderzoek der Materie FOM!, which is financially supported by the Nederlandse Organisatie voor Wetenschappelijk Onderzoek NWO!.

References

1. P.W. Anderson, Phys. Rev. **109**, 1492 (1958).
2. E. Yablonovitch, Phys. Rev. Lett. **58**, 2059 (1987).
3. S. John, Phys. Rev. Lett. **58**, 2486 (1987).
4. *Photonic crystals and light localization in the* 21^{st} *century*, edited by C.M. Soukoulis (Kluwer Academic Publishers, Dordrecht, 2001).
5. V. S. Letokhov, Sov. Phys. JETP **26**, 835 (1968).
6. N. M. Lawandy, R. M. Balachandran, A. S. L. Gomes, and E. Sauvain, Nature (London) **368**, 436 (1994).
7. H. Cao, Y. Ling, J.Y. Xu, C.Q. Cao, and P. Kumar, Phys. Rev. Lett., **86**, 4524 (2001).
8. F.J.P. Schuurmans, D. Vanmaekelbergh, J. van de Lagemaat, and A. Lagendijk,

Science **284**, 141 (1999).
9. F.J.P. Schuurmans, M. Megens, D. Vanmaekelbergh, and A. Lagendijk, Phys. Rev. Lett. **83**, 2183 (1999).
10. J. Gómez Rivas, A. Lagendijk, R.W. Tjerkstra, D. Vanmaekelbergh, and J.J. Kelly, Appl. Phys. Lett. **80**, 4498 (2002).
11. S.M. Sze, *Physics of semiconductor devices* (Wiley-intersceince, New York, 1981).
12. B.H. Erné, D. Vanmaekelbergh, and J.J. Kelly, J. Electrochem. Soc. **143**, 305 (1996).
13. J. Gómez Rivas, *Light in strongly scattering semiconductors*, PhD. thesis, University of Amsterdam (2002). Available at: http://www.tn.utwente.nl/cops/.
14. P.C. Searson, J.M. Macaulay, and F.M. Ross, J. Appl. Phys. **72**, 253 (1992).
15. X.G. Zhang, J. Electrochem. Soc. **138**, 3750 (1991).
16. J. Gómez Rivas, R. Sprik, A. Lagendijk, L.D. Noordam, and C.W. Rella, Phys. Rev. E **62**, R4540 (2000); Phys. Rev. E **63**, 046613 (2001).
17. D.S. Wiersma, M.P. van Albada, and A. Lagendijk, Rev. Sci. Instrum. **66**, 5473 (1995).
18. E. Akkermans, P.E. Wolf, and R. Maynard, Phys. Rev. Lett. **56**, 1471 (1986).
19. M.B. van der Mark, M.P. van Albada, and A. Lagendijk, Phys. Rev. B. **37**, 3575 (1988).
20. J. Gómez Rivas, D.H. Dau, A. Imhof, R. Sprik, B.P.J. Bret, P.M. Johnson, T.W. Hijmans, and A. Lagendijk, submitted (2002).
21. G. van Soest, M. Tomita, and A. Lagendijk, Opt. Lett. **24**, 306 (1999).
22. G. van Soest, F.J. Poelwijk, R. Sprik, and A. Lagendijk, Phys. Rev. Lett. **86**, 1522 (2001).
23. G. van Soest, F.J. Poelwijk, and A. Lagendijk, Phys. Rev. E **65**, 046603 (2002).
24. G. van Soest, and A. Lagendijk, Phys. Rev. E 65, 047601 (2002).
25. Gijs van Soest, *Experiments on random lasers*, PhD. thesis, University of Amsterdam (2002). Available at: http://www.tn.utwente.nl/cops/.
26. See e.g. A. E. Siegman, *Lasers*, (University Science Books, Mill Valley, 1986).
27. M. Siddique, R. R. Alfano, G. A. Berger, M. Kempe, and A. Z. Genack, Opt. Lett. **21**, 450 (1996).
28. R. M. Balachandran, N. M. Lawandy, and J. A. Moon, Opt. Lett. **22**, 319 (1997).
29. W. L. Sha, C.-H. Liu, F. Liu, and R. R. Alfano, Opt. Lett. **21**, 1277 (1996).
30. R. M. Balachandran, A. E. Perkins, and N. M. Lawandy, Opt. Lett. **21**, 650 (1996).
31. A. Yu. Zyuzin, JETP Lett. **61**, 990 (1995).
32. D. S. Wiersma, M. P. van Albada, and A. Lagendijk, Phys. Rev. Lett. **75**, 1739 (1995).
33. A. A. Burkov and A. Yu. Zyuzin, Phys. Rev. B, **55**, 5736 (1997).
34. X. Jiang and C. M. Soukoulis, Phys. Rev. B **59**, 6159 (1999).
35. G. A. Berger, M. Kempe, and A. Z. Genack, Phys. Rev. E **56**, 6118 (1997).
36. R. M. Balachandran and N. M. Lawandy, Opt. Lett. **21**, 1603 (1996).
37. S. John and G. Pang, Phys. Rev. A **54**, 3642 (1996).
38. H. Cao, J. Y. Xu, S.-H. Chang, S. T. Ho, E. W. Seelig, X. Liu, and R. P. H. Chang, Phys. Rev. Lett. **84**, 5584 (2000).
39. X. Jiang and C. M. Soukoulis, Phys. Rev. Lett. **85**, **70** (2000).
40. In the proceeding of the NATO Advanced Study Institute, 'Wave scattering in complex media; from theory to aplplication', Cargese, France, june 10-22 (2002).
41. A. Z. Genack, *Fluctuations, correlation and average transport of electromagnetic radiation in random media*, in: P. Sheng (Ed.), *Scattering and localization of classical waves in random media*, World Scientific Series on Directions in Condensed Matter Physics, vol. 8, (World Scientific, Singapore, 1990).
42. J. W. Goodman, *Statistical properties of laser speckle patterns*, sect. 2.1, 2.2 (on intensity statistics) and 2.5 (on speckle spot size) in: J. C. Dainty (Ed.), *Laser speckle and related phenomena*, 2nd ed., Topics in Applied Physics, vol. 9, (Springer, Berlin, 1984).

43. D. S. Wiersma and A. Lagendijk, Physica A **241**, 82 (1997).
44. C. Gouedard, D. Husson, C. Sauteret, F. Auzel, and A. Migus, J. Opt. Soc. Am. B **10**, 2358 (1993).
45. M. A. Noginov, S. U. Egarievwe, N. Noginova, H. J. Caulfield, and J. C. Wang, Opt. Mat. **12**, 127 (1999).
46. G. Parry, *Speckle patterns in partially coherent light*, sect. 3.1 and 3.2 in: J. C. Dainty (Ed.), *op. cit.* [42].
47. Y. Kuga and A. Ishimaru, J. Opt. Soc. Am. A **8**, 831 (1984); M. P. van Albada and A. Lagendijk, Phys. Rev. Lett. **55**, 2692 (1985); P. E. Wolf and G. Maret, *ibid.* **55**, 2696 (1985).
48. A. Yu. Zyuzin, Europhys. Lett. **26**, 517 (1994).
49. P. C. de Oliveira, A. E. Perkins, and N. M. Lawandy, Opt. Lett. **21**, 1685 (1996).
50. W. Deng, D. S. Wiersma, and Z. Q. Zhang, Phys. Rev. B **56**, 178 (1997).